

## A frequency and amplitude scanned quadrupole mass filter for the analysis of high $m/z$ ions

Deven L. Shinholt, Staci N. Anthony, Andrew W. Alexander, Benjamin E. Draper, and Martin F. Jarrold

Citation: [Review of Scientific Instruments](#) **85**, 113109 (2014); doi: 10.1063/1.4900627

View online: <http://dx.doi.org/10.1063/1.4900627>

View Table of Contents: <http://scitation.aip.org/content/aip/journal/rsi/85/11?ver=pdfcov>

Published by the [AIP Publishing](#)

---

### Articles you may be interested in

[Hybrid quadrupole mass filter/quadrupole ion trap/time-of-flight-mass spectrometer for infrared multiple photon dissociation spectroscopy of mass-selected ions](#)

*Rev. Sci. Instrum.* **82**, 054101 (2011); 10.1063/1.3585982

[Development of a high precision quadrupole mass filter using the zero-method control circuit](#)

*Rev. Sci. Instrum.* **71**, 1332 (2000); 10.1063/1.1150459

[Nonlinear field effects in quadrupole mass filters](#)

*Rev. Sci. Instrum.* **70**, 3566 (1999); 10.1063/1.1149960

[Low-cost modification for the high-frequency raster on the Cameca IMS-3F secondary ion mass spectrometer](#)

*J. Vac. Sci. Technol. A* **17**, 317 (1999); 10.1116/1.581587

[Transmission through the quadrupole mass spectrometer mass filter: The effect of aperture and harmonics](#)

*J. Vac. Sci. Technol. A* **15**, 2276 (1997); 10.1116/1.580734

---



**Not all AFMs are created equal**  
**Asylum Research Cypher™ AFMs**  
**There's no other AFM like Cypher**

[www.AsylumResearch.com/NoOtherAFMLikeIt](http://www.AsylumResearch.com/NoOtherAFMLikeIt)

**OXFORD**  
INSTRUMENTS  
*The Business of Science®*

# A frequency and amplitude scanned quadrupole mass filter for the analysis of high $m/z$ ions

Deven L. Shinholt, Staci N. Anthony, Andrew W. Alexander, Benjamin E. Draper, and Martin F. Jarrold

*Department of Chemistry, Indiana University, 800 East Kirkwood Ave., Bloomington, Indiana 47405, USA*

(Received 11 September 2014; accepted 17 October 2014; published online 21 November 2014)

Quadrupole mass filters (QMFs) are usually not used to analyze high  $m/z$  ions, due to the low frequency resonant circuit that is required to drive them. Here we describe a new approach to generating waveforms for QMFs. Instead of scanning the amplitude of a sine wave to measure the  $m/z$  spectrum, the frequency of a trapezoidal wave is digitally scanned. A synchronous, narrow-range ( $<0.2\%$ ) amplitude scan overlays the frequency scan to improve the sampling resolution. Because the frequency is the primary quantity that is scanned, there is, in principle, no upper  $m/z$  limit. The frequency signal is constructed from a stabilized base clock using a field programmable gate array. This signal drives integrating amplifiers which generate the trapezoidal waves. For a trapezoidal wave the harmonics can be minimized by selecting the appropriate rise and fall times. To achieve a high resolving power, the digital signal has low jitter, and the trapezoidal waveform is generated with high fidelity. The QMF was characterized with cesium iodide clusters. Singly and multiply charged clusters with  $z$  up to  $+5$  were observed. A resolving power of  $\sim 1200$  (FWHM) was demonstrated over a broad  $m/z$  range. Resolution was lost above 20 000 Th, partly because of congestion due to overlapping multiply charged clusters. Ions were observed for  $m/z$  values well in excess of 150 000 Th. © 2014 AIP Publishing LLC. [<http://dx.doi.org/10.1063/1.4900627>]

## INTRODUCTION

The quadrupole mass filter (QMF) was developed by Paul and co-workers in the 1950s.<sup>1–4</sup> It usually consists of four cylindrical metal rods arranged symmetrically around a central axis. Opposing rods are connected electrically, and the two orthogonal pairs receive RF signals with the opposite phase and DC voltages with the opposite polarity. The result is an  $m/z$  band pass filter, where the center of the band depends on the RF amplitude and frequency, and width of the band depends on the ratio of the peak-to-peak RF amplitude to the DC voltage between the rods. An  $m/z$  spectrum is usually measured by scanning the RF amplitude and DC voltage while keeping their ratio fixed. With this configuration, the maximum  $m/z$  value that can be attained is limited by the maximum RF amplitude that can be achieved before electrical breakdown and power consumption become concerns ( $\sim 10$  kV). The majority of commercial QMFs are limited to  $m/z$  values less than 2000 Th. To increase the maximum  $m/z$  value, the RF frequency must be lowered, which requires the construction of a new resonant circuit. The resolving power depends on the number of RF cycles experienced by the ion as it transits the QMF, so lowering the frequency decreases the resolving power.<sup>3</sup> Lowering the RF frequency also decreases the acceptance area at the entrance of the QMF, thereby lowering the signal intensity.<sup>3</sup>

Several low frequency QMFs have been described. Beuhler and Friedman used a QMF operating at 292 kHz to observe water clusters up to  $\sim 80$  000 Th with a resolving power of around 300.<sup>5,6</sup> Winger and co-workers described a similar system to study electrosprayed protein complexes up to  $\sim 45$  000 Th.<sup>7</sup>

In recent years, QMFs have become widely used in tandem mass spectrometry (MS) where multiple stages of MS are performed with ion fragmentation occurring between them. Examples include triple quadrupole<sup>8</sup> and quadrupole time-of-flight (Q-TOF) instruments, both of which are widely used for MS/MS studies. Robinson and co-workers have described a modified Waters Q-TOF with a QMF that has an  $m/z$  range that should extend up to 32 000 Th when operated at 300 kHz.<sup>9</sup>

A frequency scan, with fixed RF amplitude and DC voltage, is an alternate way of measuring the  $m/z$  spectrum to the more customary amplitude scan at fixed frequency. An advantage of the frequency scan is that there is, at least in principle, no upper  $m/z$  limit. The frequency scan was first demonstrated by Paul and Raether in 1955.<sup>1</sup> They analyzed  $\text{Rb}^+$  isotopes with a frequency sweep from 2.38 to 2.54 MHz. In 1981, Marmet and Proulx described a simple design for a frequency-scanned QMF power supply.<sup>10</sup> Their motivation was to design a power supply which would allow them to sit on the same  $m/z$  peak for a long period of time, up to a week, so that accurate photoionization thresholds could be measured. Finally, Rolando and collaborators have described a frequency scanned QMF with a 0.4–1.1 MHz range.<sup>11</sup> Its performance was evaluated with dibromomethane and a resolving power of 165 was reported.

While most attempts to implement frequency scanning QMFs have focused on low  $m/z$  ions ( $< 500$  Th), there has been at least one study of larger ions. Nie and co-workers used a frequency-swept QMF to study cytochrome c and gramicidin S (500–2000 Th).<sup>12</sup> For a frequency range of 100–400 kHz at a constant RF amplitude of  $\sim 100$  V, they

obtained a resolving power of  $\sim 200$  for doubly charged gramicidin S at 570.5 Th.

The primary concern with a frequency scanned QMF power supply is the accuracy of the frequency. The center of the  $m/z$  band transmitted by a QMF is proportional to  $1/f^2$ , so the frequency needs to be particularly well-defined or the resolving power will suffer. Being able to scan the frequency over a very wide range is also important. Commercial frequency synthesizers are unable to satisfy the accuracy and range requirements and this is why the amplitude scan has remained the method of choice for so many years.

In most cases, QMFs are driven with a signal that varies sinusoidally with time. However, they can be driven by a variety of non-sinusoidal, periodic waveforms. This flexibility allows QMF waveforms to be constructed through other means, and without the need for a resonant circuit. Richards, Huey, and Hiller first demonstrated this in 1973 when they used a square wave to analyze krypton ions. However, because of finite rise and fall times, their waveform was closer to trapezoidal than square. The duty cycle of their waveform was manipulated to eliminate the DC contribution.<sup>13,14</sup> A similar approach has been used in a linear quadrupole ion trap.<sup>15</sup>

The use of frequency scans<sup>16</sup> and non-sinusoidal<sup>17</sup> excitation has become commonplace with quadrupole ion traps. Digitally generated, arbitrary waveforms have recently become popular due to their innate flexibility in selected ion ejection. Xiong and co-workers have described a frequency-scanned quadrupole ion trap that is driven by rectangular and triangular waves.<sup>18</sup> Reilly and co-workers have used direct digital synthesis (DDS) to generate square waves with variable frequency and duty cycle to drive a linear quadrupole ion trap.<sup>19</sup> DDS technology is a type of frequency synthesizer, where arbitrary waveforms can be generated from a single base frequency. This technology is widely used in digital ion traps to create waveforms for ion trapping and ejection.<sup>20,21</sup>

In this paper we describe a new way of generating the waveforms to drive QMFs. The method uses a primary frequency scan with a superimposed, narrow-range ( $<0.2\%$ ) amplitude scan to increase the sampling resolution. The frequency signal is generated by dividing a stabilized base clock in a counter. This approach provides a precisely defined frequency signal with the lowest jitter over a broad range of frequencies but leads to a discrete set of frequency points. It is used to generate two opposite-phase trapezoidal waves which drive the QMF. With a trapezoidal wave the contribution from harmonics can be minimized by adjusting the length of the transition times. At each frequency, the amplitude and DC voltages can be varied over a narrow range to fill-in the gap between the discrete frequencies and improve the sampling resolution. Due to the way in which the waveforms are constructed, there is flexibility in selecting a combination of frequency, amplitude, and DC voltage that allows easy access to a wide  $m/z$  range in both the first and third<sup>22</sup> stability regions.

## EXPERIMENTAL APPARATUS

Figure 1 shows a schematic diagram of the experimental apparatus used to examine the performance of the QMF. Ions are generated by electrospray. The electrospray tips were

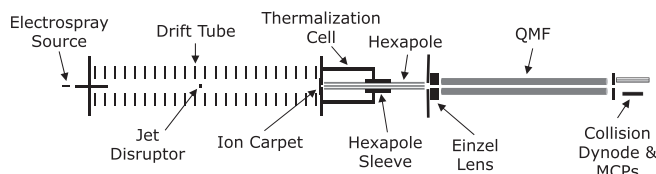


FIG. 1. Schematic diagram of the experimental apparatus used to examine the performance of the QMF.

pulled from silica capillary tubing (Polymicro, 350  $\mu\text{m}$  OD, 250  $\mu\text{m}$  ID). A syringe pump (Cole-Parmer, Model 74900) provides a constant flow of solution to the tip, and a potential of  $\sim 1.8$  kV is applied to the tip through the solution. The electrospray is sampled by a heated stainless steel capillary (0.076 cm ID), which transports ions entrained in air into the first differentially pumped region of the apparatus. The pressure in this region can be raised by admitting additional air through a leak valve. The operating pressure is typically around 700 mTorr. After exiting the capillary, a 31.6 cm long drift region consisting of 74 ring electrodes (2.54 cm ID) guides the ions towards a DC ion carpet at the other end. A jet disrupter<sup>23</sup> placed midway along the drift region blocks large droplets and disrupts the directed gas flow from the capillary. Opposite phases of an RF signal ( $\sim 300$  V peak-to-peak, 140 kHz) are applied to alternating ring electrodes to confine the ions, while a DC gradient ( $\sim 1.0$  V/cm) directs them towards the ion carpet. The DC ion carpet funnels the ions through a 0.10 cm diameter aperture into a hexapole ion guide located in the second differentially pumped region. The DC ion carpet consists of a series of concentric ring electrodes on a printed circuit board with a central exit aperture (0.10 cm ID). A DC voltage gradient across the rings (+260 V on the outer ring with the center ring grounded) funnels ions through the center aperture. No RF signals are applied. The DC ion carpet and its performance are described in detail in a recent publication.<sup>24</sup>

After the ions pass through the aperture in the DC ion carpet they enter a hexapole ion guide. The entrance end of the hexapole is enclosed to elevate the local pressure. The pressure can be adjusted over the range 30–110 mTorr by adding gas through a leak valve. The elevated pressure thermalizes the ions, removing the kinetic energy gained in the DC ion carpet and in the expansion at the exit aperture of the carpet. A 3.8 cm long conductance-limiting sleeve allows the ions to travel into a higher vacuum region ( $\sim 6.7 \times 10^{-5}$  Torr) through a gradual pressure drop while still in the hexapole. The ions then pass into the final differentially pumped region ( $\sim 1.5 \times 10^{-6}$  Torr) where an einzel lens focuses them into the QMF. The hexapole RF (200 V peak-to-peak, 285 kHz) is floated at a small DC potential (8 V) which defines the ion energy relative to the QMF pole zero (the potential on the central axis of the QMF). The quadrupole (Extrel Corp.) has nominally 9 mm diameter rods.

The performance of the QMF was examined using cesium iodide clusters. Electrospraying a CsI solution generates a wide distribution of cluster sizes and the lack of isotope distributions means that it is easy to determine the resolving power. The cesium iodide (Sigma Aldrich, 99.999%) solution was prepared at a concentration of 15 mg/ml in 50:50 water

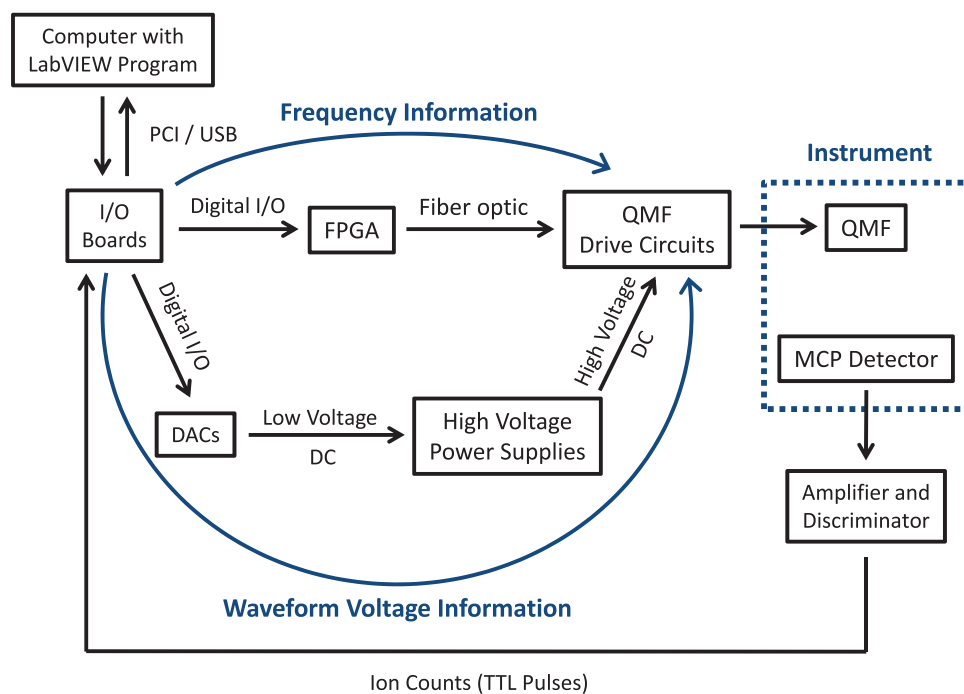


FIG. 2. Block diagram showing how information flows from the computer to the QMF drive circuit and from the ion detector to the computer. Information from the LabVIEW program about the frequency, amplitude, DC voltage, and pole zero voltage (the potential on the central axis of the QMF) is combined in the QMF drive circuit.

(EDM Millipore) and ethanol (AAPER Alcohol) and electro-sprayed at  $10 \mu\text{l/h}$ .

### QMF drive circuits

A LabVIEW (National Instruments) program controls the QMF drive circuit, inputs data from the ion detector, and generates an  $m/z$  spectrum. Figure 2 shows how information is transferred from the computer to the drive circuit. The LabVIEW program controls two I/O boards (Measurement Computing, PCI-2517 and USB-4301), which in turn communicate digitally with the home-built circuits to drive the QMF. The program communicates with a field programmable gate array (FPGA) to generate the desired frequency. The program also controls the power supplies that provide the voltages that determine the amplitude, the DC voltage, and the pole zero voltage. These voltages are generated using four low-noise DC power supplies (Matsusada Precision, Inc., RG-360-0.2) that are controlled through true 18-bit digital-to-analog converters (DAC) (Linear Technology, LTC2756) via a home-built circuit.

The desired frequency is generated by dividing a high-frequency clock in a counter. This method allows the frequency to be defined with an accuracy that is better than that of the clock because of the averaging inherent in the counting process. A high clock frequency is desirable because it gives a wider range of possible frequencies by division. The FPGA (Xilinx, Artix-7) was programmed to convert a stable ( $< 1 \text{ ps RMS phase jitter}$ ,  $\pm 50 \text{ ppm frequency stability}$ ) 200 MHz clock (SiTime Corp., SiT9102) to 570 MHz via a phase lock loop. We chose 570 MHz because it is the highest frequency that that can be reliably used with the FPGA.

The 570 MHz was divided in the FPGA by a 24 bit number provided by the LabVIEW program via the I/O boards. In this configuration, the FPGA is acting as a high-speed digital counter. This is in contrast to DDS, where the clock and a DAC are used to build an arbitrary sinusoidal waveform, which is then converted back into a rectangular waveform by a comparator. The desired frequency is sent to the QMF drive circuits via a fiber. For reasons that will become clear below, the frequency sent to the drive circuits is twice the frequency of the resulting trapezoidal waves.

A trapezoidal wave was chosen to drive the QMF because it approximates a sine wave and has much smaller harmonic contributions than a square wave. Ringing can also cause problems with a square wave. For a trapezoidal wave, the harmonics are minimized when the fraction of the period spent transitioning from peak-to-peak is twice the period spent at the peak voltage. When this occurs, the third harmonic vanishes and the contribution from all higher order harmonics is less than 10% of the fundamental.

Figure 3 shows a functional diagram of the QMF drive circuit. The drive circuit can be divided into two main constituents: the slew rate control and the rail-to-rail integrating amplifiers. The slew rate control calculates a voltage that is proportional to the desired slope of the trapezoidal waveform. The integrating amplifiers then use this voltage to generate the final waveform. The whole process is described in more detail below. The QMF drive circuits are mounted inside a stainless steel box within the vacuum chamber. The box is located directly underneath the QMF to minimize noise and load capacitance.

In the slew rate control, a fiber optic receiver converts the signal from the FPGA into a TTL signal. This signal triggers a monostable multivibrator, which allows a brief current

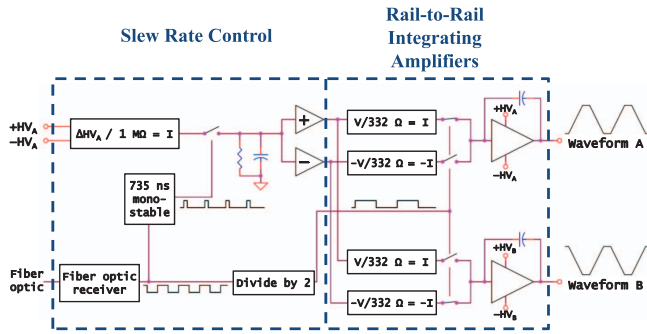


FIG. 3. Functional diagram of the QMF drive circuit. The circuit is divided into two portions, the slew rate control and the rail-to-rail integrating amplifiers. The circuit combines information about the frequency, amplitude, DC voltage, and pole zero voltage to generate the two trapezoidal waves that drive the QMF.

pulse to flow through a gated transistor. The amplitude of the current pulse is proportional to the amplitude of the trapezoidal waveform that is to be generated. A filter averages the current pulses which are then converted to inverted and non-inverted DC voltages. These voltages define the slopes of the trapezoidal wave. The magnitude of the DC voltages depends on both the frequency and amplitude to be generated. In addition to the slew rate voltages, the frequency from the FPGA is divided by two and sent to the integrating amplifiers.

In the second part of the circuit, the slew rate voltages are converted into currents and integrated by rail-to-rail integrating amplifiers. The two power supply rails of each amplifier represent the high and low voltages for that phase. These voltages are calculated in the LabVIEW program from the desired amplitude, DC voltage, and pole zero voltage, and then set using the 18 bit DACs that control the low-noise DC power supplies.

Consider one cycle to illustrate how the waveform is generated. The output starts at the negative rail. The divided frequency signal switches the polarity of the current source, so that the output voltage starts to increase linearly. It reaches the positive rail in a third of a cycle and sits there for a sixth of a cycle when the divided frequency changes state and switches the polarity of the current source. The output voltage starts to decrease linearly reaching the negative rail in a third of a cycle. It sits there for a sixth of a cycle whereupon the whole process repeats.

Ions that pass through the QMF are detected with a collision dynode ( $-7$  kV) and a pair of microchannel plates (MCPs) (Photonis Inc.) in a chevron configuration (see Figure 1). The signal from MCPs is amplified in a fast pulse preamplifier and further processed by an amplifier and discriminator. TTL pulses from the discriminator are counted in one of the 20 MHz counters on the USB-4301 I/O board. To measure an  $m/z$  spectrum, the frequency is stepped and at each frequency the signal from the detector is counted for a preset time (50 ms) and then the sum is transferred to the computer. At the end of the scan an  $m/z$  spectrum is generated in the computer and displayed.

## The relationship between frequency and $m/z$

The theory of QMF operation has been documented since the late 1950s.<sup>2</sup> Mathieu's equations describe ion motion within the oscillating and stationary fields of a QMF using two reduced parameters,  $a$  and  $q$ :

$$a = \frac{4zeU_{DC}}{mr_o^2\Omega^2}, \quad (1)$$

$$q = \frac{2zeV_{RF}}{mr_o^2\Omega^2}. \quad (2)$$

In the above equations,  $e$  is the electronic charge,  $z$  is the number of charges on the ion,  $m$  is the mass of the ion,  $r_o$  is the inscribed radius of the quadrupole rods,  $U_{DC}$  is the DC voltage between the sets of rods,  $V_{RF}$  is the peak-to-peak amplitude, and  $\Omega$  is the angular frequency. An  $a$ - $q$  stability diagram is the usual way of representing the combinations of oscillating and static fields that generate stable trajectories through a QMF (see below).

Equation (2) can be rearranged to generate an expression showing the dependence of the transmitted  $m/z$  on the amplitude and frequency ( $f$ ):

$$m/z = \frac{eV_{RF}}{2\pi^2r_o^2m_uqf^2}. \quad (3)$$

Note that we have introduced the atomic mass constant ( $m_u$ ) so that  $m$  is now in units of Daltons. The frequency is scanned to generate an  $m/z$  spectrum by incrementing the divide-by number, and so the allowed values of the frequency are given by

$$f = \frac{f_{clock}}{2n}, \quad (4)$$

where  $f$  is the generated frequency,  $n$  is the divide-by number, and  $f_{clock}$  is the frequency of the clock (570 MHz). The factor of 2 in Eq. (4) is due to the frequency divider in the QMF drive circuits (see above). Combining Eqs. (3) and (4), we see that  $m/z$  is directly proportional to  $n^2$ ,

$$m/z = \frac{eV_{RF}}{2\pi^2r_o^2m_uq} \left( \frac{2n}{f_{clock}} \right)^2. \quad (5)$$

Setting  $\Delta(m/z) = m/z(n+1) - m/z(n)$  we obtain the difference in  $m/z$  for neighboring sampling points:

$$\Delta(m/z) = 4k[k + (m/z)^{1/2}], \quad (6)$$

where

$$k = \frac{1}{\pi r_o f_{clock}} \left( \frac{eV_{RF}}{2m_uq} \right)^{1/2}. \quad (7)$$

Since  $(m/z)^{1/2} \gg k$ , the spacing between sampled  $m/z$  values increases with  $(m/z)^{1/2}$ . This is in contrast to an amplitude scan, where the  $m/z$  is linearly related to the amplitude and so the spacing is constant. Using typical values for the quantities in Eqs. (6) and (7),  $\Delta(m/z)$  is around 3 Th at  $10^3$  Th and rises to around 30 Th at  $10^5$  Th. However, note that the sampling resolving power,  $(m/z)/\Delta(m/z)$ , also scales as  $(m/z)^{1/2}$ , and it is better at higher  $m/z$ . It is desirable to reduce the separation between the sampling points (i.e., improve the sampling resolution) for all  $m/z$  values. One way to achieve this goal

is to increase the clock frequency. However, we are already operating at the maximum frequency that can be used with the FPGA, and a significantly higher frequency is not easy to achieve. Operating the QMF in the third stability region effectively doubles the sampling density, but with a significant decrease in signal intensity. Lowering the amplitude will also increase the sampling density, but ions will be transmitted at a lower frequency, and consequently lower resolving power. Direct digital synthesis (DDS) provides a means to adjust the frequency with finer resolution.<sup>19,20</sup> However, jitter is a concern with DDS methods and we did not pursue DDS because it is more difficult to implement than the method adopted below.

### A synchronized frequency and amplitude scan

As described above, the frequency scan employed here leads to a series of discrete frequency points. One approach to increasing the sampling point density is to build a narrow-range amplitude scan on top of the frequency scan. If the amplitude is adjusted slightly at a particular frequency, an  $m/z$  value between the discrete frequencies can be sampled. In the work described here, we used this approach to sample  $m/z$  values halfway between those accessed by the frequency scan (effectively halving the scanning resolution). However, there is no reason why this approach should be limited to just a single point.

Figure 4 illustrates the sequence of events when the  $m/z$  is scanned through a synchronized frequency and amplitude scan. In this case, data is collected at two amplitudes, the nominal and the adjusted value, before the frequency is incremented. The frequency and amplitude have a different dependence on  $m/z$ , so to keep the adjusted  $m/z$  points approximately halfway between those obtained with the nominal amplitude, the adjusted amplitude changes during a frequency scan (it is larger at larger frequency and hence smaller  $m/z$ ). Equation (6) is used to calculate the amplitude needed to shift the sampled  $m/z$  values. The amplitude shift is  $<0.2\%$  for the frequency range accessible in a normal scan (see below). As the amplitude is adjusted, the DC voltage between the rods is also adjusted to keep the  $a/q$  ratio (and hence the resolving

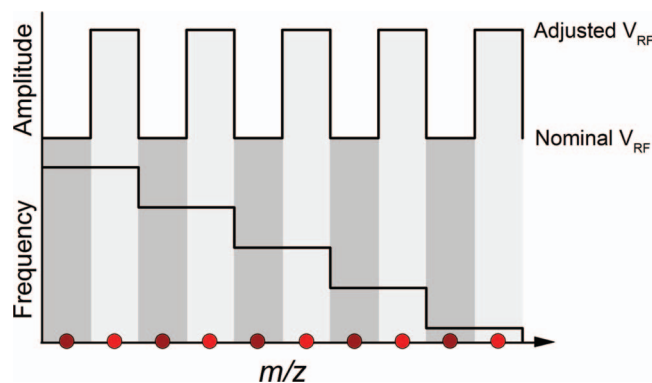


FIG. 4. Diagram illustrating how a narrow-range amplitude scan is built on top of a frequency scan. In this case, measurements are made at two amplitudes for each frequency, doubling the  $m/z$  sampling point density. The red points represent the  $m/z$  values that are sampled.

power) constant during the scan. In the future, a more sophisticated algorithm will be written so that we can select multiple amplitude values for a particular frequency, thereby sampling even more  $m/z$  values.

The  $m/z$  values accessible in a synchronized frequency and amplitude scan are restricted because the amplitude and DC voltages are incremented in units of  $\sim 1.4$  mV by the 18-bit DACs used to control the power supplies. This quantization constrains the possible amplitude values that can be selected to shift the  $m/z$ , although this only becomes detrimental at very high  $m/z$ , where the amplitude changes are very small. Another consequence of the discrete output voltages is that it is not possible to keep the ratio of the amplitude to DC voltage exactly the same throughout a scan. However, the ratio varies over a very narrow range ( $\pm 0.004\%$ ) for the  $m/z$  values of interest.

### Simulation of the stability diagram for a QMF driven by a trapezoidal wave

An  $a$ - $q$  stability diagram shows the combinations of oscillating and static fields that lead to stable trajectories. Information from the stability diagram is needed to set the resolving power (i.e., set the ratio of the DC voltage to the amplitude) and to transform the frequencies and amplitudes to an  $m/z$  scale. Previous studies have shown that stability regions with non-sinusoidal waveforms shift relative to that for a sine wave.<sup>13,25</sup> SIMION 8.1 was used to map the first stability region for the trapezoidal wave used here. First the fraction of ions transmitted was determined as a function of the DC voltage between the rods for a range of  $q$ -values. The derivative of each transmission plot was then calculated and plotted. The DC offset at the point of greatest change was deemed to be the point of instability, so the DC offset directly preceding this value was assigned to be the limit of the stability region. Once the DC offset at each  $q$ -value was determined for the edge of the stability region, the corresponding  $a$ -values were calculated. The regions were then plotted (see Figure 5). The same approach was used to map the first stability region for a sine wave and square wave and the results are shown in Figure 5 for comparison. All three stability regions show similar roughly triangular shapes. ( $q, a$ ) points within the triangle are stable solutions, while those outside are unstable. QMFs are usually operated near the apex of the triangle. The apex of the first stability region for the sine wave was found to be at (0.706, 0.230), which is in good agreement with the actual value (0.70601, 0.23697).<sup>2</sup> The apex for the simulated square wave was found to be (0.553, 0.231). This can be compared to the location found by Richards and co-workers, which was (0.586, 0.237).<sup>13</sup> The discrepancy between the  $q$ -values probably results from the imperfect square wave used by Richards and co-workers. It had long rise and fall times so it was closer to trapezoidal.<sup>13</sup> A value of  $\sim 0.55$  has recently been reported for the  $q$ -value of a square wave.<sup>26</sup> This is in good agreement with the value we deduced from trajectory calculations. The apex of the stability diagram for the trapezoid wave used here was found to be (0.670, 0.230). Notice that the stability diagram for the trapezoidal wave is closer to the sine wave than the square wave. This is expected because the trapezoidal

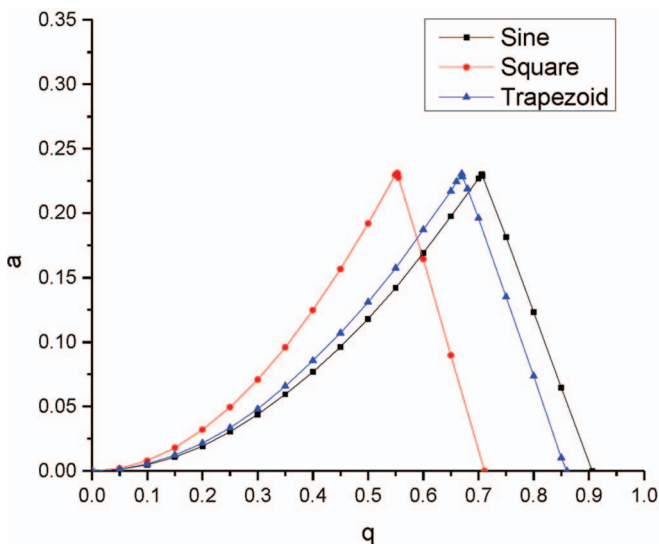


FIG. 5. First stability regions for sine (black), square (red), and trapezoid (blue) waveforms determined from SIMION simulations. Equations for the reduced parameters  $a$  and  $q$  are given in the text.

wave used here was optimized to minimize harmonics and hence provide the best approximation to a sine wave. In the experiments described below, the  $q$ -value of the apex for the trapezoidal wave is used to provide an initial calibration for the  $m/z$  scale and the  $a$ -value at the apex is used as a guide to set the resolving power.

## EXPERIMENTAL RESULTS

We start by discussing the  $m/z$  range that is accessible with the QMF drive circuit. The response of the filter in the slew rate control (see Figure 3) determines the lowest frequency that can be reliably accessed with the QMF drive circuit. This is currently 12 kHz. Using this frequency with a peak-to-peak amplitude of 400 V leads to an upper  $m/z$  limit of  $\sim 1.2$  MTh. This upper limit could be extended by small modifications to the filter. The high frequency limit of the drive circuits (which sets the low  $m/z$  limit) is determined by the width of the current pulses in the slew rate control (see Figure 3). The limit is currently  $\sim 500$  kHz. Reducing the current pulse length in the drive circuit would raise the high frequency limit. With a frequency of 500 kHz and a peak-to-peak amplitude of 400 V the lower  $m/z$  limit is  $\sim 700$  Th. This limit can be lowered by lowering the amplitude or by operating in the third stability region (or both). With an amplitude of 200 V the lower  $m/z$  limit is  $\sim 350$  Th and in the third stability region with the same amplitude the limit is  $\sim 80$  Th.

It is necessary to convert the frequency scale that is used to measure the data, to an  $m/z$  scale. This transformation was initially performed using the stability diagram simulations described above. Specifically, we used the  $q$ -value at the apex of the first stability region for the trapezoidal wave (0.670) to provide an initial calibration. The  $m/z$  scale was then refined using the known masses of the measured peaks. This led to an experimental value for  $q$  at the apex of 0.651. This is in good agreement with the value from the simulations which is around 3% smaller.

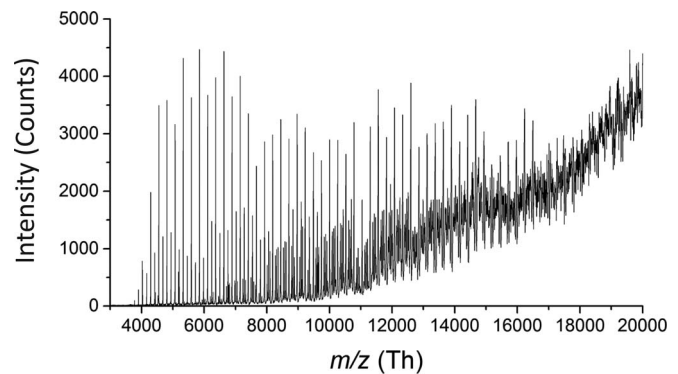


FIG. 6.  $m/z$  spectrum measured for CsI clusters up to 20000 Th. Peaks due to the  $(\text{CsI})_n\text{Cs}^+$  sequence are evident up to  $\sim 16500$  Th.

Electrosprayed CsI clusters were studied to investigate the performance of the QMF over a wide range of  $m/z$  values. The pressures in the first and second differentially pumped regions were found to be critical for the efficient transmission of large ions.<sup>9,27</sup> If the pressures are too low, large ions are not properly thermalized; if they are too high, the ions diffuse away and are lost. All  $m/z$  spectra shown here were collected in the first stability region with an amplitude of 200 V peak-to-peak.

Figure 6 shows a typical  $m/z$  spectrum measured for CsI clusters up to 20000 Th. The positively charged CsI clusters observed in this work consist of a number of CsI units along with one or more excess  $\text{Cs}^+$  ions that provide the overall charge. Singly charged clusters occur at  $m/z$  values corresponding to  $(\text{CsI})_n\text{Cs}^+$  and doubly charged clusters occur at  $m/z$  values corresponding to  $(\text{CsI})_{2n}\text{Cs}_2^{2+}$  and  $(\text{CsI})_{2n+1}\text{Cs}_2^{2+}$ . The doubly charged  $(\text{CsI})_{2n}\text{Cs}_2^{2+}$  clusters have the same  $m/z$  as the singly charged  $(\text{CsI})_n\text{Cs}^+$  clusters, while the  $m/z$  for doubly charged  $(\text{CsI})_{2n+1}\text{Cs}_2^{2+}$  ions lies halfway between two neighboring singly charged clusters. Triply charged clusters have  $m/z$  values corresponding to the following combinations:  $(\text{CsI})_{3n}\text{Cs}_3^{3+}$ ,  $(\text{CsI})_{3n+1}\text{Cs}_3^{3+}$ , and  $(\text{CsI})_{3n+2}\text{Cs}_3^{3+}$ . The triply charged  $(\text{CsI})_{3n}\text{Cs}_3^{3+}$  have the same  $m/z$  as singly charged  $(\text{CsI})_n\text{Cs}^+$  and doubly charged  $(\text{CsI})_{2n}\text{Cs}_2^{2+}$ , while the other triply charged clusters,  $(\text{CsI})_{3n+1}\text{Cs}_3^{3+}$  and  $(\text{CsI})_{3n+2}\text{Cs}_3^{3+}$ , occur at  $m/z$  values 1/3 and 2/3 of the way between two neighboring singly charged clusters. The situation for more highly charged clusters follows the pattern outlined above.

In Figure 6 there is a progression of peaks due to a sequence of  $(\text{CsI})_n\text{Cs}^+$  ions that extends up to  $\sim 16501$  Th ( $n = 63$ ). Above 16500 Th, the peaks belonging to this sequence are difficult to distinguish from the background. For low  $m/z$  values, the  $(\text{CsI})_n\text{Cs}^+$  peaks are due to singly charged clusters, but for higher  $m/z$  values multiply charged clusters:  $(\text{CsI})_{2n}\text{Cs}_2^{2+}$ ,  $(\text{CsI})_{3n}\text{Cs}_3^{3+}$ , etc. (which have the same  $m/z$ ) become increasingly important. When the pressures in the first and second differentially pumped regions are lowered to encourage low  $m/z$  transmission, singly charged clusters can be observed all the way down to  $\text{Cs}^+$  (132.9 Th). Doubly charged clusters emerge at  $(\text{CsI})_{21}\text{Cs}_2^{2+}$  (2861 Th), which is in good agreement with the size range predicted for the emergence of doubly charged alkali halide clusters in the

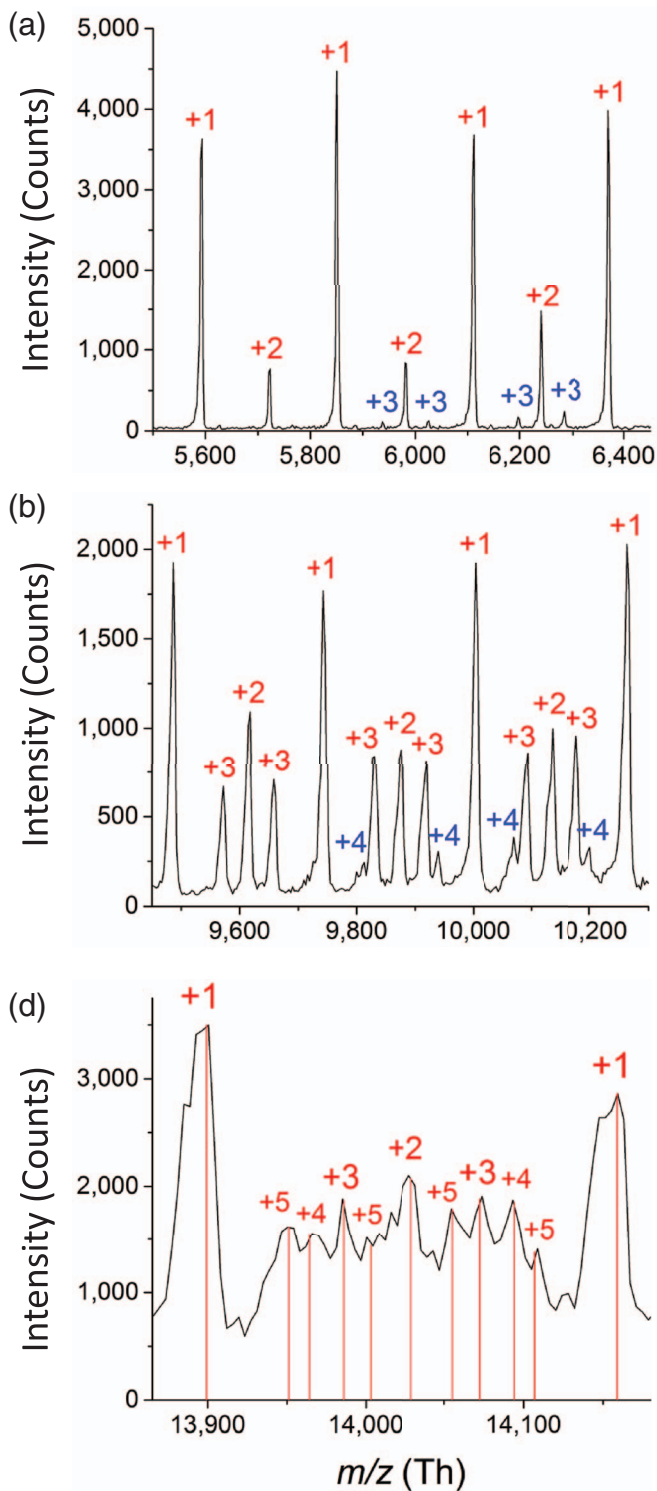


FIG. 7. (a) Expanded view of the  $m/z$  spectrum around 6000 Th showing the onset of clusters with a charge of +3, beginning with  $(\text{CsI})_{67}\text{Cs}_3^{3+}$  at 5935 Th. (b) Expanded view of the  $m/z$  spectrum around 10000 Th showing the onset of clusters with a charge of +4, beginning with  $(\text{CsI})_{149}\text{Cs}_4^{4+}$  at 9811 Th. (c) Expanded view of the  $m/z$  spectrum around 14000 Th showing the presence of overlapping charge states up to +5.

calculations of Martin.<sup>28</sup> Figure 7(a) is an expanded view of the  $m/z$  spectrum around 6000 Th that shows the onset of triply charged CsI clusters at 5935 Th. Singly and doubly charged clusters are easily identified in this  $m/z$  range. Figure 7(b) shows the onset of quadruply charged CsI clus-

ters at 9811 Th. Note that the sums of the intensities of the doubly charged peaks due to  $(\text{CsI})_{2n+1}\text{Cs}_2^{2+}$  ions (which are labelled +2 in the figure) and the triply charged peaks due to  $(\text{CsI})_{3n+1}\text{Cs}_3^{3+}$  or  $(\text{CsI})_{3n+2}\text{Cs}_3^{3+}$  ions (labelled +3) are comparable to the intensities of the peaks at the positions expected for singly charged  $(\text{CsI})_n\text{Cs}^+$  clusters (labelled +1). This suggests that the peaks labelled +1 in Figure 7(b) are mainly due to doubly charged  $(\text{CsI})_{2n}\text{Cs}_2^{2+}$  ions and triply charged  $(\text{CsI})_{3n}\text{Cs}_3^{3+}$  ions, and the amount of singly charged  $(\text{CsI})_n\text{Cs}^+$  ions is small at these  $m/z$  values.

Well-resolved multiply charged clusters are easily identified up to  $\sim 12000$  Th. At larger  $m/z$  values, higher charge states appear, resolution among the multiple charge states is lost, and the baseline increases. Figure 7(c) shows a narrow portion of the spectrum around  $m/z$  14000 Th where  $(\text{CsI})_n\text{Cs}_z^{z+}$  clusters up to  $z = 5$  have been identified. At this point, the peaks labelled +1 could have contributions from  $(\text{CsI})_n\text{Cs}^+$ ,  $(\text{CsI})_{2n}\text{Cs}_2^{2+}$ ,  $(\text{CsI})_{3n}\text{Cs}_3^{3+}$ ,  $(\text{CsI})_{4n}\text{Cs}_4^{4+}$ ,  $(\text{CsI})_{5n}\text{Cs}_5^{5+}$ , etc. which all have the same  $m/z$ . Although, the contributions from the singly charged  $(\text{CsI})_n\text{Cs}^+$  clusters, and probably also the doubly charged  $(\text{CsI})_{2n}\text{Cs}_2^{2+}$  clusters, are small at this  $m/z$  and it is mainly higher charge states that are responsible for the peaks labelled +1 in Figure 7(c).

For  $m/z$  values between 16500 and 20000 Th, it is still possible to identify peaks at  $m/z$  values corresponding to the  $(\text{CsI})_n\text{Cs}^+$  sequence. However, beyond 20000 Th the assignments become unreliable, and the peaks submerge into the background that first appears at  $\sim 10000$  Th and grows with increasing  $m/z$ . This background is probably the result of unresolved multiply charged clusters as well as clusters that are incompletely desolvated or contain impurities. Figure 8 shows a spectrum measured for  $m/z$  values up to 200000 Th. In this spectrum, there is a broad feature centered around 30000 Th and another centered around 90000 Th. The centers of these features can be manipulated by adjusting the pressure in the thermalization cell, the hexapole frequency, and the hexapole and QMF pole zero potentials. They do not contain resolved peaks so the chemical nature cannot be determined; however, they are expected to be predominantly multiply charged cesium iodide nanocrystals.

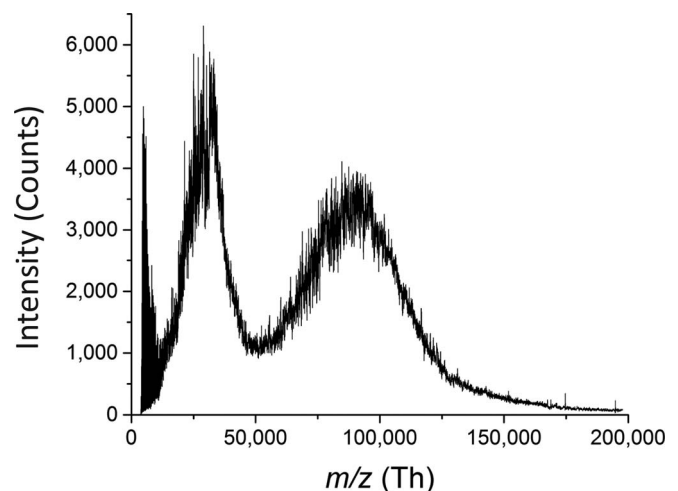


FIG. 8. An  $m/z$  spectrum measured up to 200000 Th.

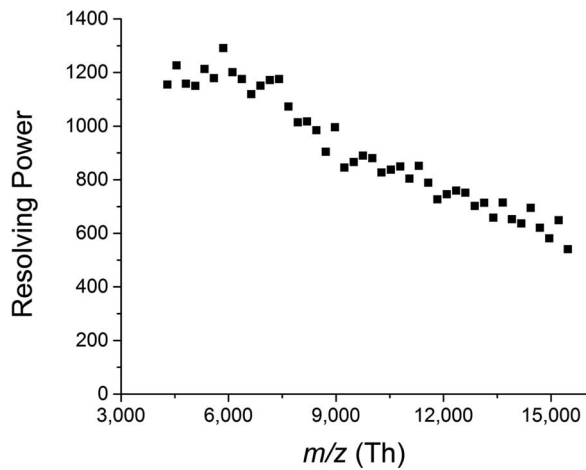


FIG. 9. Resolving power (FWHM) determined for the  $(\text{CsI})_n\text{Cs}^+$  sequence of peaks as a function of  $m/z$ .

The resolving power,  $(m/z)/\Delta(m/z)$ , was determined for the peaks corresponding to the  $(\text{CsI})_n\text{Cs}^+$  sequence in the  $m/z$  spectrum. At low  $m/z$  these peaks are mainly due to singly charged clusters, but multiply charge  $(\text{CsI})_n\text{Cs}_z^{z+}$  clusters become dominant at higher  $m/z$ . Each peak was fit with a Gaussian function using OriginPro 9.0 and then the FWHM was determined from the standard deviation. The resolving powers are plotted against  $m/z$  in Figure 9. The resolving power remains constant (approximately 1200) up to  $\sim 7500$  Th, and then gradually drops to  $\sim 600$  at 15 000 Th.

If the ratio of the amplitude of the trapezoidal wave to the DC offset is fixed, and with  $a$  and  $q$  values close to the tip of the stability diagram, the resolving power is expected to be proportional to  $N^2$  where  $N$  is the number of cycles experienced by the ions as they travel through the QMF.<sup>3</sup> If the ions all had the same velocity, as the frequency is lowered, the number of cycles they experience would decrease. However, the ions do not have the same velocity; ideally, they have the same energy per charge (because they are all accelerated through the same potential difference before entering the QMF). Equation (8) relates the number of cycles an ion experiences to the frequency, the potential difference ( $V$ ) through which the ions are accelerated, and the length of the QMF ( $L$ ):

$$N = Lf \left( \frac{m/z}{2eV} \right)^{1/2}. \quad (8)$$

It is evident from Eq. (3) that  $m/z$  is proportional to  $1/f^2$ ; consequently, the number of cycles the ions experience when they are transmitted by the QMF is constant. Hence the resolving power should be independent of frequency and  $m/z$ .<sup>11</sup> With a constant resolving power, the resolution scales as  $(m/z)$ . As noted above, the spacing between the frequency sampling points changes as  $(m/z)^{1/2}$  so the number of sampling points across a peak increases as  $(m/z)^{1/2}$ . In other words, for a constant resolving power there are more sampling points across the peaks at high  $m/z$  than low  $m/z$ .

Experimentally, we found that the resolving power remained constant up to  $\sim 7500$  Th and then started to decrease. We attribute this decrease to the large ions entering the

QMF with excess kinetic energy. This causes the large ions to travel through the QMF more quickly, experience fewer cycles, and consequently the resolving power is lower. The presence of excess kinetic energy was confirmed by experiments where the QMF was operated as a crude retarding potential difference energy analyzer whereby the pole zero was raised (made more positive) until the ion signal disappeared. We are performing simulations to identify the cause of the excess kinetic energy and ultimately find a way to eliminate it. Incomplete dehydration and impurities probably also contribute to the widths of the peaks at high  $m/z$  values.

The transmission of an ion through a QMF depends on the entrance conditions (position and velocities) and the phase of the RF. Increased resolving power is usually associated with a decreased overall transmission efficiency. With a frequency scan, the overall transmission efficiency (at fixed energy/charge) is independent of the frequency and  $m/z$  for the same reason that the resolving power is independent of frequency and  $m/z$ : the change in the frequency needed to transmit ions with different  $m/z$  but with the same energy/charge is exactly compensated by the change in the velocities. In contrast, for a traditional amplitude scan, the transmission efficiency for ions with the same energy/charge, decreases as the  $m/z$  increases.

## CONCLUSIONS

We have described a new approach to scanning a quadrupole mass filter using a primary frequency scan with a superimposed, narrow-range amplitude scan to increase the sampling resolution. Because the frequency is the primary quantity scanned, the upper  $m/z$  limit can be made arbitrarily large. Trapezoidal waves are used to generate the oscillating electric fields in the QMF. With a trapezoidal waveform the contribution from harmonics can be minimized by adjusting the length of the transition times. The  $m/z$  resolving power is much better than has been obtained with a frequency scan in the past. The main factors responsible for the improved resolving power are that we have implemented the simultaneous frequency/amplitude scan and we have taken great care to ensure that the uncertainty in the frequency is small. The frequency signal is digitally generated from a stabilized base clock. The computer interface and the digital design of the QMF drive circuits allow great flexibility, where the frequency, amplitude, and DC voltage are all easily adjusted variables. This flexibility allows the operator to choose the stability region and to simultaneously scan the frequency, amplitude, and DC voltage.

## ACKNOWLEDGMENTS

We gratefully acknowledge the support of the National Science Foundation through Grant No. 0832651. We are grateful for the technical assistance of Mr. John Poehlman in Electronic Instrumentation Services and Mr. Delbert Allgood in Mechanical Instrument Services in the Indiana University Chemistry Department.

- <sup>1</sup>W. Paul and M. Raether, "Das elektrische massenfilter," *Z. Phys.* **140**, 262–273 (1955).
- <sup>2</sup>W. Paul, H. P. Reinhard, and U. von Zahn, "Das elektrische massenfilter als massenspektrometer und isotopentrenner," *Z. Phys.* **152**, 143–182 (1958).
- <sup>3</sup>P. H. Dawson, *Quadrupole Mass Spectrometry and Its Applications* (Elsevier, Amsterdam, 1976).
- <sup>4</sup>D. J. Douglas, "Linear quadrupoles in mass spectrometry," *Mass Spectrom. Rev.* **28**, 937–960 (2009).
- <sup>5</sup>R. J. Beuhler and L. Friedman, "Threshold studies of secondary electron emission induced by macro ion impact on solid surfaces," *Nucl. Instrum. Methods* **170**, 309–315 (1980).
- <sup>6</sup>R. J. Beuhler and L. Friedman, "A study of the formation of high molecular weight water cluster ions ( $m/e < 59000$ ) in expansion of ionized gas mixtures," *J. Chem. Phys.* **77**, 2549–2557 (1982).
- <sup>7</sup>B. E. Winger, K. J. Light-Wahl, R. R. Ogorzalek Loo, H. R. Udseth, and R. D. Smith, "Observation and implications of high mass-to-charge ratio ions from electrospray ionization mass spectrometry," *J. Am. Soc. Mass Spectrom.* **4**, 536–545 (1993).
- <sup>8</sup>R. A. Yost and C. G. Enke, "Selected ion fragmentation with a tandem quadrupole mass spectrometer," *J. Am. Chem. Soc.* **100**, 2274–2275 (1978).
- <sup>9</sup>F. Sobott, H. Hernandez, M. G. McCammon, M. A. Tito, and C. V. Robinson, "A tandem mass spectrometer for improved transmission and analysis of large macromolecular assemblies," *Anal. Chem.* **74**, 1402–1407 (2002).
- <sup>10</sup>P. Marmet and M. Proulx, "A frequency-swept quadrupole mass filter," *Int. J. Mass Spectrom. Ion Proc.* **42**, 3–10 (1982).
- <sup>11</sup>B. Landais, C. Beaugrand, L. Capron-Dukan, M. Sablier, G. Simonneau, and C. Rolando, "Varying the radio frequency: A new scanning mode for quadrupole analyzers," *Rapid Commun. Mass Spectrom.* **12**, 302–306 (1998).
- <sup>12</sup>Z. X. Nie, C. W. Lin, W. P. Peng, Y. T. Lee, and H. C. Chang, "Frequency scan of a quadrupole mass analyzer in the third stability region for protein analysis," *J. Chin. Chem. Soc.* **53**, 47–52 (2006).
- <sup>13</sup>J. A. Richards, R. M. Huey, and J. Hiller, "A new operating mode for the quadrupole mass filter," *Int. J. Mass Spectrom. Ion Phys.* **12**, 317–339 (1973).
- <sup>14</sup>J. A. Richards, R. M. Huey, and J. Hiller, "Waveform parameter tolerances for the quadrupole mass filter with rectangular excitation," *Int. J. Mass Spectrom. Ion Phys.* **15**, 417–428 (1974).
- <sup>15</sup>F. L. Brancia, B. McCullough, A. Entwistle, J. G. Grossmann, and L. Ding, "Digital asymmetric waveform isolation (DAWI) in a digital linear ion trap," *J. Am. Soc. Mass Spectrom.* **21**, 1530–1533 (2010).
- <sup>16</sup>U. P. Schlunegger, M. Stoeckli, and R. M. Caprioli, "Frequency scan for the analysis of high mass ions generated by matrix-assisted laser desorption/ionization in a Paul trap," *Rapid Commun. Mass Spectrom.* **13**, 1792–1796 (1999).
- <sup>17</sup>L. Ding, M. Sudakov, and S. Kumashiro, "A simulation study of the digital ion trap mass spectrometer," *Int. J. Mass Spectrom.* **221**, 117–138 (2002).
- <sup>18</sup>C. Q. Xiong, G. P. Xu, X. Y. Zhou, J. N. Wang, Y. Tang, R. Chen, W. P. Peng, H. C. Chang, and Z. X. Nie, "The development of charge detection-quadrupole ion trap mass spectrometry driven by rectangular and triangular waves," *Analyst* **137**, 1199–1204 (2012).
- <sup>19</sup>H. Koizumi, B. Jatko, W. H. Andrews, Jr., W. B. Whitten, and P. T. A. Reilly, "A novel phase-coherent programmable clock for high-precision arbitrary waveform generation applied to digital ion trap mass spectrometry," *Int. J. Mass Spectrom.* **292**, 23–31 (2010).
- <sup>20</sup>L. Ding, M. Sudakov, F. L. Brancia, R. Giles, and S. Kumashiro, "A digital ion trap mass spectrometer coupled with atmospheric pressure ion sources," *J. Mass Spectrom.* **39**, 471–484 (2004).
- <sup>21</sup>M. Yang, T.-Y. Kim, H.-C. Hwang, S.-K. Yi, and D.-H. Kim, "Development of a palm portable mass spectrometer," *J. Am. Soc. Mass Spectrom.* **19**, 1442–1448 (2008).
- <sup>22</sup>S. U. A. H. Syed, T. J. Hogan, M. J. Antony Joseph, S. Maher, and S. Taylor, "Quadrupole mass filter: Design and performance for operation in stability zone 3," *J. Am. Soc. Mass Spectrom.* **24**, 1493–1500 (2013).
- <sup>23</sup>T. Kim, K. Tang, H. R. Udseth, and R. D. Smith, "A multicapillary inlet jet disruption electrodynamic ion funnel interface for improved sensitivity using atmospheric pressure ion sources," *Anal. Chem.* **73**, 4162–4170 (2001).
- <sup>24</sup>S. N. Anthony, D. L. Shinholt, and M. F. Jarrold, "A simple electrospray interface based on a DC ion carpet," *Int. J. Mass Spectrom.* **371**, 1–7 (2014).
- <sup>25</sup>N. V. Kononov, M. Sudakov, and D. J. Douglas, "Matrix methods for the calculation of stability diagrams in quadrupole mass spectrometry," *J. Am. Soc. Mass Spectrom.* **13**, 597–613 (2002).
- <sup>26</sup>G. F. Brabeck and P. T. A. Reilly, "Mapping ion stability in digitally driven ion traps and guides," *Int. J. Mass Spectrom.* **364**, 1–8 (2014).
- <sup>27</sup>I. V. Chernushevich and B. A. Thomson, "Collisional cooling of large ions in electrospray mass spectrometry," *Anal. Chem.* **76**, 1754–1760 (2004).
- <sup>28</sup>T. P. Martin, "Stability of doubly charged alkali halide clusters," *J. Chem. Phys.* **76**, 5467–5469 (1982).